Tip tilt and focus estimation based on LGS and downlink joint measurements for ground to GEO satellite optical communication link

PERRINE LOGNONÉ,[1,2,3,*] GHAYA REKAYA,[2] AURÉLIE MONTMERLE-BONNEFOIS,[1] LAURIE PAILLIER,[1] AND JEAN-MARC CONAN[1]

[1]*ONERA, DOTA, Paris-Saclay University, F-92322 Châtillon, France*
[2]*Télécom Paris, LTCI, 19 pl. Marguerite Perey, 91120 Palaiseau, France*
[3]*Centre for Advanced Instrumentation, Department of Physics, Durham University, Durham DH1 3LE, UK*
[*]perrine.l.lognone@durham.ac.uk

Abstract: Achieving high data rates in GEO Feeder optical uplinks faces challenges due to the fading nature of the channel induced by atmospheric turbulence. Adaptive optics pre-compensation using downlink measurements is a solution to mitigate the impact of the turbulence. However, the point-ahead angle anisoplanatism, inherent to the bidirectional link geometry, limits the uplink correction efficiency, leading to persistent signal fades and loss of information onboard the satellite. We recently proposed a new minimum mean square error method that improves the phase estimation at the PAA based on the downlink phase and log amplitude measurements, reducing the anisoplanatism impact on the coupled flux. Alternatively, a laser guide star can be used to measure the phase at the PAA. However, it is currently challenging to retrieve the tip, tilt, and focus modes, whose correction is essential to improve the link quality. In this article, we propose to combine both techniques to estimate the tip, tilt, and focus at the PAA by incorporating the LGS high-order measurements in the MMSE formalism. We develop the associated analytical reconstructor and evaluate the performance of the phase estimation and the gain on the coupled flux statistics aboard the GEO satellite, considering an idealized LGS system. The new estimator is shown to reduce the tip, tilt, and focus error variances by up to 70% of their initial value.

1. Introduction

In the digital era where the demand for data communication keeps increasing, satellite communication is an appealing solution to complement the terrestrial communication infrastructures. In this space network, geostationary (GEO) satellites aim at being nodes connecting the core terrestrial network to the satellite network [1]. Therefore, the link between the Earth and the GEO satellite must support very high data rates. To meet these very high data-rate requirements, using optical wavelength is envisioned, offering a large communication bandwidth, while overcoming the radio-frequencies allocation and data-rates bottleneck. Indeed, using the optical bands C+L would allow communicating over an 11 THz large bandwidth [2], and enable data rates in the order of several Terabits per second. However, to achieve these data rates, issues such as the mitigation of the impact of atmospheric turbulence on the optical link, still need to be solved.

Indeed, the phase and amplitude of optical beams are impaired by turbulence when they propagate through the atmosphere which induces random fluctuations of the flux coupled to an optical system. Hence, both the GEO-to-ground (down) and ground-to-GEO (up) optical links suffer from deep attenuations induced by atmospheric turbulence. To mitigate these random signal fluctuations, it is currently foreseen to correct the phase with an adaptive optics (AO)

system. In particular, in the uplink scenario, the current solution is to pre-compensate the beam at its emission [3]. The efficiency of the AO pre-compensation strongly depends on the choice of the applied AO correction. The most mature technique demonstrated in the field, consists in using the downlink beam correction to pre-compensate the uplink [4–9]. However, because of the inherent point-ahead angle (PAA) separating the downlink and uplink optical paths, the phase disturbances encountered by both beams are different, and this uplink pre-compensation is suboptimal. The phase error induced by the pre-compensation of the beam at the PAA by the downlink phase measured at the angular reference 0 is called phase anisoplanatism and leads to residual beam wander and beam pattern distortions in the satellite plane. Hence, the received signal onboard the satellite still undergoes long and deep fades.

Alternatively, to improve the uplink pre-compensation, it was proposed by Tyson [3] to use a reference downlink beacon at the PAA to perform the AO correction, that could be provided by a laser guide star (LGS). Whilst not demonstrated yet in the framework of space optical communication links, this method was proved theoretically to improve the uplink correction [10,11] and led to the development of several projects (currently running [12–14]) aiming at demonstrating the feasibility of uplink phase pre-compensation aided by LGS sensing. However, one of the main issues currently faced by the LGS solution is the tip-tilt and focus indetermination [15], meaning that these modes cannot be accurately measured on the LGS beacon. As the correction of these modes, especially the tip and tilt, is crucial to limit the beam wander effect in the satellite plane and limit the signal fades, there is still a need to find solutions to correct the uplink tip, tilt and focus.

Several methods have been proposed in the literature to retrieve the tip-tilt from the laser guide star. Among these, differential methods, by using either the time delay propagation of the LGS signal [16], the sodium structures anisotropies [17,18] or polychromatic guide stars [19], could lead to absolute tip-tilt retrieval. However, whilst under demonstration [20], the implementation of these methods is challenging, and, to our knowledge, no quantification of these methods' efficiency in the telecom scenario could be found.

A second family of methods, based on the statistical estimation of the phase at the PAA, including the tip, tilt and focus, can be found in the literature. A first method, issued from Whiteley's work, consists in estimating the LGS tip, tilt and focus using the LGS high-order phase measurements and statistical priors with an MMSE estimation [21]. We also proposed, in earlier work, to estimate the phase at the PAA for a system without LGS. The technique consists in computing an MMSE estimator using the downlink phase and log-amplitude measurements and statistical priors [11,22]. It was already shown to significantly decrease the tip, tilt and focus pre-compensation phase error in severe atmospheric conditions.

Hence, in the aim to further improve the estimation of the pre-compensation phase at the point-ahead angle with an additional source of information, we propose, in this article, to combine the MMSE phase estimation proposed in [22] with the LGS-based tip, tilt and focus estimation of Whiteley [21], using solely the LGS phase modes that can be measured at the OGS. In this aim, we build a new estimator of the tip, tilt and focus at the PAA jointly exploiting the on-axis downlink beam phase, the on-axis downlink log-amplitude, and the LGS phase high order measurements, and statistical priors.

We start in section 2 by presenting the GEO Feeder link system, the LGS system geometry, and the modelling hypotheses. We construct the new analytical estimator in section 3, and demonstrate its efficiency in section 4 in terms of phase modal reduction and improvement of the coupled flux statistics, considering an idealised LGS system. We also compute the link capacity improvement compared to state-of-the-art pre-compensation techniques. These results are calculated for a full range of representative atmospheric conditions.

2. System model

2.1. Reciprocal model of the ground to GEO link

2.1.1. Link geometry

We consider a bidirectional optical link between an optical ground station and a GEO satellite at $30°$ elevation, hence located 38000 km above Earth, as depicted in Fig. 1. The atmosphere close to the ground, is approximately 40 km thick. The downlink and uplink optical paths are separated by the point-ahead angle α_{PAA}. We set the downlink path axis as the angular reference such that $\alpha = 0$. Hence, the uplink optical axis is located at $\alpha = \alpha_{PAA}$ as shown in Fig. 1.

An AO system corrects in real-time the phase perturbations of the downlink beam after propagation through turbulence before single mode fibre (SMF) injection at the OGS and pre-compensates the uplink with a given correction phase. When using the classical pre-compensation method mentioned in the introduction, the pre-compensation phase equals the downlink AO correction phase. In the following, we consider a simplified AO system, accounting only for the fitting error (phase error due to the limited number of AO correction modes), and the anisoplanatic error, induced by the downlink and uplink paths angular difference, that are the dominant phase error terms in the pre-compensated uplink scenario. We choose an AO system with 135 correction modes (from mode 2, tip, to mode 136), that we express in the Zernike polynomial basis [23].
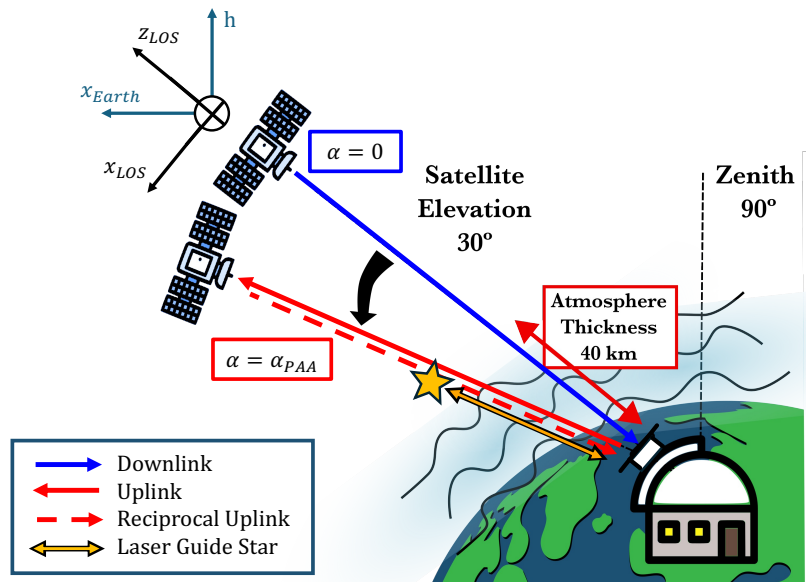

Fig. 1. Illustration of the bidirectional GEO satellite to Earth system. The downlink is depicted in blue, the uplink and reciprocal uplink in red and the LGS in orange.

We consider a communication link at the telecom wavelength 1550 nm. We also assume that the downlink and the uplink are received and emitted through the same telescope aperture, whose diameter is equal to 60 cm. The OGS and AO system parameters are synthesised in Table 1.

To ease the analysis of the uplink pre-compensation phase error, we adopt a reciprocal formalism as in [22,24,25]. Uplink pre-compensation is indeed equivalent to the correction on the ground of the phase experienced by the reciprocal uplink, being a downlink at the PAA, as described in Fig. 1. Therefore, we can express both the downlink and the reciprocal uplink in the OGS aperture as: $\Psi(\mathbf{r}, t; \alpha) = A_0 \exp\left(\chi(\mathbf{r}, t; \alpha) + j\Phi(\mathbf{r}, t; \alpha)\right)$ where $\mathbf{r}$ is the spatial coordinates

Table 1. Parameters describing the ground to satellite optical pre-compensated link.

	Link, OGS and AO Parameters
Satellite elevation	30 $^\circ$
Point-ahead angle (α_{PAA})	18.5 µrad
Wavelength Tx/Rx (λ)	1550 nm
Telescope diameter (D_{tel})	60 cm
AO modes highest index (N_{AO})	136 (up to radial order $n_r = 15$)

vector in the OGS aperture, Φ is the turbulent phase, χ depicts the log-amplitude fluctuations of the complex field, and A_0 is the amplitude constant term.

2.1.2. Reciprocal coupled flux definition

The reciprocal formalism, not only allows for the expression of the reciprocal uplink beam in the OGS aperture using a plane wave formalism but also enables computing the coupling efficiency, as demonstrated in [24,26,27]. It states that the coupled flux of an emitted mode, after propagation, to a reception mode (at z=L), is equal to the coupled flux of the back-propagated reception mode to the emission mode (at z=0). Therefore, we compute the coupled flux onboard the satellite of the pre-compensated uplink as the coupled flux at the OGS of the reciprocal uplink (that is the satellite reception mode back-propagated toward the OGS at the PAA), corrected by AO, to the laser emission mode:

$$f_{pre-compensated,OGS \rightarrow satellite}(t) = f_{satellite \rightarrow OGS,compensated}(t) \tag{1}$$

$$= \frac{\left| \iint \exp(\chi(\mathbf{r},t;\alpha_{PAA}) + j\Phi_{res}(\mathbf{r},t))M_0(\mathbf{r})d^2r \right|^2}{\iint |M_0(\mathbf{r})|^2 \, d^2\mathbf{r}} \tag{2}$$

where $\Phi_{res}(\mathbf{r},t) = \Phi(\mathbf{r},t;\alpha_{PAA}) - \Phi_{AO}(\mathbf{r},t)$ is the reciprocal uplink residual phase after AO correction, and $M_0(\mathbf{r})$ denote the Gaussian laser Tx mode. In the following, we study the statistics of the coupled flux, hence, we neglect the time t and the physical quantities χ, Φ_{res} and f are considered as random variables.

2.2. Laser guide star system and model

We consider a sodium LGS, which is the chosen system in recent demonstrators for uplink pre-compensation [12,14], as it limits the cone effect [28] due to the high altitude of the sodium layer (~90 km above Earth). This sodium LGS is generated by a laser that excites the sodium layer in the atmosphere, allowing wavefront measurements in the desired direction from the back-propagated photons emitted during the atoms' deexcitation.

The LGS is an extended source at a finite distance on the axis at α_{PAA}, as depicted in Fig. 1. The source extension implies that we can only measure the phase from the LGS, and not the scintillation [29]. As mentioned above, this system provides a wavefront measurement in the direction of interest. However, it can't measure the tip and tilt aberrations so far. Additionally, the focus aberration cannot be measured with accuracy. This is due to the fluctuation in time and space of the sodium layer concentration [18]. Hence, we assume that only the phase high order modes (astigmatism and beyond), can be measured from the LGS at the PAA.

In our developments, the LGS is supposed to be monostatic, and we assume that the LGS launch beam is pre-compensated with the phase measured from the satellite downlink, to limit the LGS beam wander and the spot width. We then assume that the LGS phase high-orders are perfectly measured, discarding errors induced by spot wander and source extension.

Finally, due to the height of the LGS (90 km at zenith, 180 km at 30 ° elevation), and the small LGS Rx diameter, we neglect the cone effect and model the LGS phase statistics using a plane wave formalism. We note that, as such LGS system with a small Rx aperture is not considered in the literature, to our knowledge, the hypotheses of neglecting the cone effect will be verified in section 4.4.

To summarise, we model the LGS phase measurements as perfect phase measurements obtained from a plane wave at the PAA, excluding tip, tilt and focus, as in [21].

3. Proposed estimator

In this section, we describe the proposed MMSE estimator relying on the downlink phase and log-amplitude, and LGS phase high-orders measurements and statistical priors. We start by defining the general notations used in the estimator development. Next, we develop the estimator using the Zernike modal formalism. Finally, we specify the measurement vector and the covariance matrices necessary to compute the analytical estimator.

3.1. General notations

Following [22], we express the phase and log-amplitude, in a vector formalism, as their expansion onto the Zernike polynomial basis, as:

$$\mathbf{\Phi}_\alpha = \begin{bmatrix} a_2^\alpha & \cdots & a_N^\alpha \end{bmatrix}^T \quad \text{and} \quad \chi_\alpha = \begin{bmatrix} b_1^\alpha & \cdots & b_N^\alpha \end{bmatrix}^T \tag{3}$$

where N is the Noll index [23] of the last polynomial used in the expansion, and a_i^α and b_i^α are the ith projections of the phase and log-amplitude of the beam received from the axis at angle α, respectively.

Additionally, we define the cross-covariance matrix between the two physical quantities X and Y associated with the vectors $\mathbf{X}$ and $\mathbf{Y}$, separated by the angle α as:

$$\Gamma_{XY}(\alpha) = \mathbb{E}[\mathbf{XY}^T] = [\mathbb{E}[x_i^\alpha y_j^\alpha]]_{i_0 \leq i \leq i_N, j_0 \leq j \leq j_N}, \tag{4}$$

where i_0, i_N and j_0, j_N, are the first and last index of X and Y, respectively. This cross-covariance matrix simplifies as an autocovariance when $X = Y$ and $\alpha = 0$.

3.2. Tip tilt and focus MMSE estimator

3.2.1. General MMSE estimator

Following [22], the general phase error on the tip, tilt and focus for an estimator linear with the measurements can be expressed as:

$$\mathbf{e} = \mathbf{\Phi}_{res,TTF} = \mathbf{\Phi}_{PAA,TTF} - \mathbf{Ry}_m, \tag{5}$$

where R is the linear reconstructor, $\mathbf{y}_m$ is the measurement vector, and

$$\mathbf{\Phi}_{PAA,TTF} = \begin{bmatrix} a_2^{\alpha_{PAA}} & a_3^{\alpha_{PAA}} & a_4^{\alpha_{PAA}} \end{bmatrix}^T \tag{6}$$

is the PAA phase low order modes (tip, tilt and focus) vector, where the terms $a_i^{\alpha_{PAA}}$ are the phase Zernike coefficients of the ith mode.

The general phase error covariance matrix on the subset of AO corrected modes can be expressed as:

$$\mathbf{\Gamma_{res,TTF}} = \mathbb{E}[\mathbf{ee}^T] = \mathbf{\Gamma}_{\Phi\Phi}(0) - \mathbf{R\Gamma}_{\Phi y_m}(\alpha_{PAA})^T - \mathbf{\Gamma}_{\Phi y_m}(\alpha_{PAA})\mathbf{R}^T + \mathbf{R\Gamma}_{y_m y_m}(0)\mathbf{R}^T \tag{7}$$

where $\mathbf{\Gamma_{res,TTF}} \in \mathbb{R}^{3 \times 3}$, $\mathbf{\Gamma}_{\Phi\Phi}(0)$ is the autocovariance matrix of the tip, tilt and focus, $\mathbf{\Gamma}_{\Phi y_m}(\alpha_{PAA})$ is the covariance matrix of the off-axis tip, tilt and focus and the on-axis measurement vector, and $\mathbf{\Gamma}_{y_m y_m}(0)$ is the autocovariance matrix of the measurement vector.

MMSE estimation [22,30], is given by the following reconstructor:

$$\mathbf{R}_{MMSE} \triangleq \operatorname{argmin}_{\mathbf{R}} \mathbb{E}[\mathbf{e}^T \mathbf{e}] = \mathbf{\Gamma}_{\Phi y_m}(\alpha_{PAA}) \mathbf{\Gamma}_{y_m y_m}(0)^{-1} \tag{8}$$

Additionally, the associated estimation error covariance matrix reads, applying Eq. (7) and Eq. (8):

$$\mathbf{\Gamma}_{AO,res-MMSE} = \mathbf{\Gamma}_{\Phi\Phi}(0) - \mathbf{R}_{MMSE} \mathbf{\Gamma}_{\Phi y_m}(\alpha_{PAA})^T \tag{9}$$

3.2.2. Measurement vector specification

In previous work, we only used the on-axis downlink phase and log-amplitude measurements to estimate the phase at the PAA [22]. We now introduce the LGS off-axis phase high-order measurements in the measurement vector, now defined as:

$$\mathbf{y}_m = \begin{bmatrix} \mathbf{\Phi}_0^T & \mathbf{\chi}_0^T & \mathbf{\Phi}_{\alpha_{PAA},HO}^T \end{bmatrix}^T, \tag{10}$$

where the high order phase (astigmatism and beyond) at point ahead angle is described as:

$$\mathbf{\Phi}_{\alpha_{PAA},HO}^T = \begin{bmatrix} a_5^{\alpha_{PAA}} & \cdots & a_{N_{LGS}}^{\alpha_{PAA}} \end{bmatrix}^T, \tag{11}$$

and where the on-axis measured phase and log-amplitude are expressed as:

$$\mathbf{\Phi}_0^T = \begin{bmatrix} a_2^0 & \cdots & a_{N_{AO}}^0 \end{bmatrix}^T \quad \text{and} \quad \mathbf{\chi}_0^T = \begin{bmatrix} b_1^0 & \cdots & b_{N_{AO}}^0 \end{bmatrix}^T. \tag{12}$$

Hence, the measurement vector $\mathbf{y}_m$ has the dimensions $[(N_{AO} - 1) + N_{AO} + (N_{LGS} - 4)] \times 1$. We note that the highest index of the modes measured on the downlink N_{AO} can be different from the LGS sensed modes' highest index N_{LGS}.

Thanks to this new error criterion and measurement vector, we can derive the MMSE reconstructor by defining the covariance matrix between the tip, tilt and focus at the point-ahead angle and the measurement vector and the autocovariance of the measurement vector.

The covariance matrix between the tip-tilt-focus at the point-ahead angle and the measurement vector is computed as:

$$\mathbf{\Gamma}_{\Phi_{TTF}y_m}(\alpha_{PAA}) = \begin{bmatrix} \mathbf{\Gamma}_{\Phi_{TTF}\Phi}(\alpha_{PAA}) & \mathbf{\Gamma}_{\Phi_{TTF}\chi}(\alpha_{PAA}) & \mathbf{\Gamma}_{\Phi_{TTF}\Phi_{HO}}(0) \end{bmatrix}, \tag{13}$$

where $\mathbf{\Gamma}_{\Phi_{TTF}y_m}(\alpha_{PAA}) \in \mathbb{R}^{3 \times ((N_{AO}-1)+N_{AO}+(N_{LGS}-4))}$.

Moreover, we define the autocovariance of the measurement vector as:

$$\mathbf{\Gamma}_{y_m y_m}(0) = \begin{bmatrix} \mathbf{\Gamma}_{\Phi\Phi}(0) & \mathbf{\Gamma}_{\Phi\chi}(0) & \mathbf{\Gamma}_{\Phi\Phi_{HO}}(\alpha_{PAA}) \\ \mathbf{\Gamma}_{\chi\Phi}(0) & \mathbf{\Gamma}_{\chi\chi}(0) & \mathbf{\Gamma}_{\chi\Phi_{HO}}(\alpha_{PAA}) \\ \mathbf{\Gamma}_{\Phi_{HO}\Phi}(\alpha_{PAA}) & \mathbf{\Gamma}_{\Phi_{HO}\chi}(\alpha_{PAA}) & \mathbf{\Gamma}_{\Phi_{HO}\Phi_{HO}}(0) \end{bmatrix}, \tag{14}$$

where $\mathbf{\Gamma}_{y_m y_m}(0) \in \mathbb{R}^{((N_{AO}-1)+N_{AO}+(N_{LGS}-4)) \times ((N_{AO}-1)+N_{AO}+(N_{LGS}-4))}$.

Knowing the two covariance matrices, and applying Eq. (8), we can compute the MMSE estimator, that we name: $MMSE_{\Phi\chi,LGS}$. The formulas for computing the covariance matrix coefficients can be found in [22] and rely on the knowledge of the turbulence C_n^2 profile. This analytical formalism is constructed assuming the turbulence is within the Rytov regime.

4. Results

4.1. Numerical framework

To emulate the reciprocal uplink corrected by adaptive optics in the Rytov regime, we use a pseudo-analytical model presented in [27]. This model assumes the independence between the phase and the log-amplitude contribution to the coupling, such that the coupled flux can be expressed as :

$$f = \rho_\Phi \rho_\chi, \tag{15}$$

where ρ_Φ and ρ_χ denote the phase and log-amplitude induced coupled flux fluctuations, respectively.

We assume the aperture averaged scintillation to dominate the log-amplitude contribution ρ_χ. Therefore, ρ_χ is expressed as [27,31]:

$$\rho_\chi = e^{-\sigma_\chi^2} e^{-2\chi_{Ap}}, \tag{16}$$

where $e^{-\sigma_\chi^2}$ is a static penalty term to account for the spatial log-amplitude fluctuations [32,33], and σ_χ^2 denotes the log-amplitude variance and equals to:

$$\sigma_\chi^2 = 0.5631 k_0^{7/6} \int_0^L C_n^2(z) z^{5/6} dz, \tag{17}$$

where k_0 is the wave number and $C_n^2(z)$ is the turbulence profile at distance z from the OGS aperture. Additionally, χ_{Ap} is the log-amplitude averaged by the pupil random variable that follows a Normal distribution $\mathcal{N}(-\sigma_{\chi_{Ap}}^2, \sigma_{\chi_{Ap}}^2)$, whose variance is computed as [34,35]:

$$\sigma_{\chi_{Ap}}^2 = 5.20 R_{tel}^{5/3} k_0^2 \int_0^L dz C_n^2(z) \int_0^\infty dk k^{-14/3} J_1(k)^2 \sin^2\left(\frac{zk^2}{2k_0^2 R_{tel}^2}\right), \tag{18}$$

where R_{tel} is the telescope aperture radius and J_1 is the Bessel function of the first kind of order 1. Hence, we can draw an arbitrarily large number of random occurrences of χ_{Ap} and compute ρ_χ.

Additionally, the phase contribution to the coupling ρ_Φ is expressed as:

$$\rho_\Phi = \iint \exp(j\Phi_{res}(\mathbf{r})) M_0(\mathbf{r}) P(\mathbf{r}) d\mathbf{r}^2 \cdot \exp(-\sigma_{super-fitting}^2), \tag{19}$$

where Φ_{res} is a random variable that can be represented on the Zernike polynomial basis by the random vector $\boldsymbol{\Phi}_{res}$, up to the mode highest modelled index N_{max} taken greater than N_{AO} so as to both represent the anisoplanatic and the fitting phase error. The residual phase vector covariance matrix is then expressed in the general case as [27]:

$$\boldsymbol{\Gamma}_{\Phi_{res}} = \begin{bmatrix} [\boldsymbol{\Gamma}_{\Phi_{res,AO}}]_{2 \le i,j \le N_{AO}} & \mathbf{0} \\ \mathbf{0} & [\boldsymbol{\Gamma}_{\Phi\Phi}(0)]_{N_{AO}+1 \le i,j \le N_{max}} \end{bmatrix}, \tag{20}$$

where $\boldsymbol{\Gamma}_{\Phi_{res,AO}}$ is the covariance matrix of the AO corrected phase at the PAA, and $\boldsymbol{\Gamma}_{\Phi\Phi}(0)$ is the covariance matrix of the uncorrected phase.

Hence, knowing that the residual phase vector follows a centred Normal law $\mathcal{N}(\mathbf{0}, \boldsymbol{\Gamma}_{\Phi_{res}})$ [36], we can draw the phase residual Zernike coefficients, and numerically reconstruct the field and the overlap integral with the Gaussian mode $M_0(\mathbf{r})$, whose waist is set equal to $\omega_0 = 2R_{tel}/2.2$ [31]. In addition, the super-fitting term $\sigma_{super-fitting}^2 = 0.458(n_{r,max} + 1)^{-5/3} \left(\frac{D}{r_0}\right)^{5/3}$ [37] is a static term

accounting for the modes not represented over the Zernike polynomial basis, where $n_{r,max}$ is the radial order associated to the mode highest order N_{max}.

To summarise, the simulation steps consist in: computing the residual phase covariance matrix, drawing the Zernike coefficients whose statistics are driven by this covariance matrix, synthesising the numerical reciprocal complex field and performing the overlap integral with the Tx Gaussian mode of the laser and applying the phase static losses term, to obtain the phase coupling efficiency ρ_Φ. Meanwhile, ρ_χ is calculated by drawing the scalar χ_{Ap} samples, and apply Eq. (16). Finally, the coupled flux f is obtained by multiplying ρ_χ and ρ_Φ, as stated in Eq. (15).

In the following simulations, we compute 50000 independent coupled flux samples for each atmospheric scenario considered. We also compute the phase covariance matrix for modes ranging from 2 to $N_{max} = 497$.

4.2. Atmospheric parameters

To study the estimator in several atmospheric conditions, we consider a set of C_n^2 profiles constructed from database measurements, that we call MOSPAR-XY profiles [38,39]. These profiles are composite profiles created from astronomical site measurement databases. These profiles, described in detail in [4,39], are constructed based on the statistical distributions of two key parameters: the isoplanatic angle θ_0, which characterises the angular decorrelation of turbulence, and the Fried parameter r_0, which reflects the strength of phase perturbation. The thresholds X and Y are applied to these statistical distributions, such that $P(\theta_0 < \theta_{0,th}) = X/100$ and $P(r_0 < r_{0,th}) = Y/100$. For instance, the profile MOSPAR9090 has an isoplanatic angle and a Fried parameter that are more severe than 90% of the database profiles.

In this work, we consider a set of MOSPAR profiles where $X = Y \in \{10, 20, 30, 40, 50, 60, 70, 80, 90, 99\}$. As an illustration, we plotted the MOSPAR profiles 1010, 5050 and 9999 as a function of the distance to the OGS in Fig. 2.
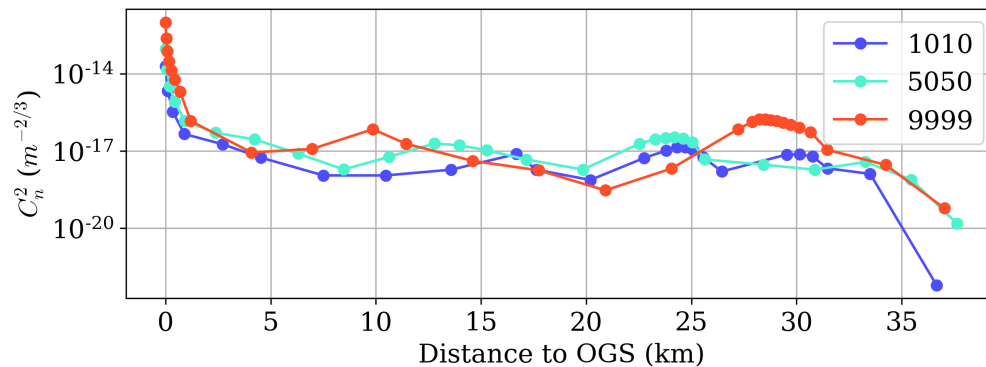

Fig. 2. Refractive index structure constant C_n^2 function of the distance to the OGS aperture, for the MOSPAR-XY profiles corresponding to the thresholds 1010, 5050 and 9999.

Figure 3 depicts the integrated parameters of the considered profiles. We plot the Fried parameter r_0 function of the isoplanatic angle θ_0. The r_0 parameter belongs to the range 16.32 cm in the MOSPAR 1010 case to 2.62 cm in the MOSPAR 9999 case, and θ_0 to the range 17.76 μrad to 4.82 μrad. Although not depicted on the graph, the log-amplitude variance σ_χ^2 ranges from 0.01 to 0.19, which confirms that we can consider being in the Rytov regime.

Additionally, we consider an outer scale $L_0 = 20\,m$. This is a typical value found in the literature from measurement campaigns [40].
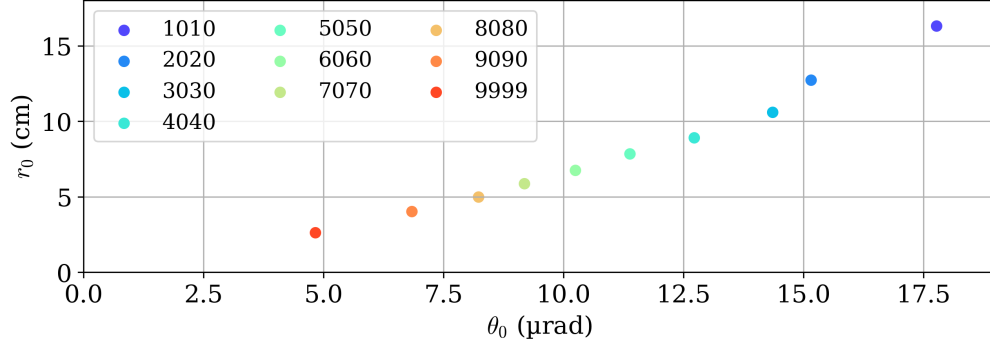
Fig. 3. Integrated parameters for all the considered MOSPAR profiles computed at 1550 nm and 30 ° elevation.

4.3. Benchmark cases

We compare the results to benchmark cases from the state-of-the-art. The first benchmark case is the classical pre-compensation, whose AO correction is the same as the downlink correction. In this case, the residual phase vector writes:

$$\mathbf{\Phi}_{res,AO_{classic}} = \mathbf{\Phi}_{\alpha_{PAA}} - \mathbf{\Phi}_0, \tag{21}$$

and its residual phase covariance matrix is equal to:

$$\mathbf{\Gamma}_{res,AO_{classic}} = 2\mathbf{\Gamma}_{\Phi\Phi}(0) - \mathbf{\Gamma}_{\Phi\Phi}(\alpha_{PAA}) - \mathbf{\Gamma}_{\Phi\Phi}^T(\alpha_{PAA}) \tag{22}$$

where $\mathbf{\Gamma}_{\Phi\Phi}(\alpha)$ is the phase angular covariance matrix that can be computed using the equations in [22].

The second benchmark case is the standard LGS case. In this case, we assume a perfect correction of the high-order modes and apply the downlink correction to the tip, tilt and focus. Hence, the residual phase vector writes:

$$\mathbf{\Phi}_{res,AO_{LGS}} = \mathbf{\Phi}_{\alpha_{PAA}} - \begin{bmatrix} [\mathbf{\Phi}_0]_{2 \leq i \leq 4} \\ [\mathbf{\Phi}_{\alpha_{PAA}}]_{5 \leq i \leq N_{AO}} \end{bmatrix}, \tag{23}$$

and its residual phase covariance matrix is equal to:

$$\mathbf{\Gamma}_{res,AO_{LGS}} = \begin{bmatrix} [\mathbf{\Gamma}_{res,classic}]_{2 \leq i,j \leq 4} & \mathbf{0} \\ \mathbf{0} & \mathbf{0} \end{bmatrix} \tag{24}$$

Finally, the last benchmark case is the estimated correction at the PAA using only the downlink phase and log-amplitude measurements, denoted as the $MMSE_{\Phi\chi}$ method, proposed in [22]. In this case, the residual phase vector writes:

$$\mathbf{\Phi}_{res,MMSE_{\Phi\chi}} = \mathbf{\Phi}_{\alpha_{PAA}} - \mathbf{R}_{MMSE_{\Phi\chi}} \mathbf{y}_m \tag{25}$$

where $\mathbf{y}_m = \begin{bmatrix} \mathbf{\Phi}_0^T & \mathbf{\chi}_0^T \end{bmatrix}^T$, and $\mathbf{R}_{MMSE_{\Phi\chi}}$ is computed accordingly to Eq. (8). The associated residual phase covariance matrix is written as:

$$\mathbf{\Gamma}_{res,MMSE_{\Phi\chi}} = \mathbf{\Gamma}_{\Phi\Phi}(0) - \mathbf{R}_{MMSE_{\Phi\chi}} \mathbf{\Gamma}_{\Phi y_m}^T(\alpha_{PAA}). \tag{26}$$

We illustrate the residual phase modal spectrum function of the Zernike mode for $N_{AO} = 136$, for the three benchmark cases described above in Fig. 4, in the MOSPAR 9090 turbulent scenario.

The classic is plotted in black, the LGS correction case in green stars, and the $MMSE_{\Phi\chi}$ case in blue. These modal variances will be used to generate the coupled flux statistics, as described in section 4.1. We highlight the tip-tilt residual variance asymmetry. This asymmetry can be explained by the link geometry. In the chosen convention, the tip is oriented in the direction of the PAA. Therefore, the phase difference between two spatially separated beam footprints in this direction is greater than in the transverse (tilt) direction.
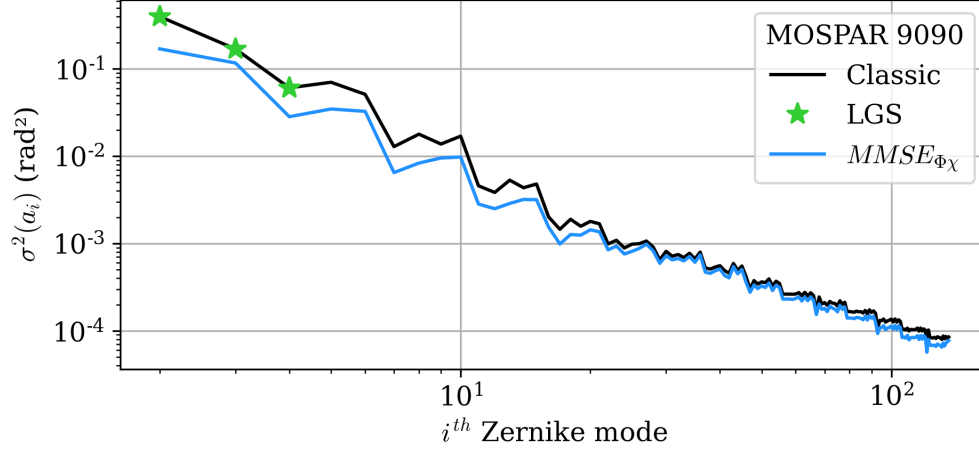
Fig. 4. Residual modal phase variance function of the Zernike mode, for the state-of-the-art cases that are: the classical pre-compensation (black), the standard LGS with classical pre-compensation on the tip, tilt and focus (green) (high-order modes of the phase are assumed to be fully corrected), and the $MMSE_{\Phi\chi}$ technique (blue).

4.4. LGS cone effect assumption validation

In this section, we verify the assumption of modelling the LGS return signal as a plane wave, in the case of small apertures, which corresponds to neglect the cone effect.

The phase error induced by the cone effect results from the phase difference issued from the wavefront LGS conic projection to a plane wave wavefront (that is the one to correct). To quantify this phase difference, we compute the variance of the modal phase error between the plane wave received at the PAA and the spherical wave at the PAA, as defined in [41,42]:

$$\mathbf{\Gamma}_{cone} = \mathbb{E}[(\mathbf{\Phi}_{\alpha_{PAA},PW} - \mathbf{\Phi}_{\alpha_{PAA},SP})^T (\mathbf{\Phi}_{\alpha_{PAA},PW} - \mathbf{\Phi}_{\alpha_{PAA},SP})] \tag{27}$$

$$= \mathbf{\Gamma}_{\Phi_{PW}\Phi_{PW}}(0) + \mathbf{\Gamma}_{\Phi_{SP}\Phi_{SP}}(0) - \mathbf{\Gamma}_{\Phi_{PW}\Phi_{SP}}(0) - \mathbf{\Gamma}_{\Phi_{SP}\Phi_{PW}}(0) \tag{28}$$

where $\mathbf{\Phi}_{\alpha_{PAA},PW}$ denotes the plane wave phase at α_{PAA} and $\mathbf{\Phi}_{\alpha_{PAA},SP}$ the phase issued from a spherical wave at α_{PAA}. To compute the different terms, we use the formalism described in [11,22,43], by applying a variable radius $R_2(z) = R_{tel}(1 - z/z_{LGS})$, where z the distance to the OGS aperture, where z_{LGS} is the LGS distance and R_{tel} is the telescope radius, to account for the LGS conic projection. We evaluate the impact on the high-order modes, excluding tip, tilt and focus, for $R_{tel} = 30 \, cm$. We plot on the right of Fig. 5 the phase variance of the cone error on the high order modes, that is the trace of Γ_{cone} starting to astigmatism and beyond, for every turbulence condition. It is compared to the turbulent phase variance of the high-order modes and to the anisoplanatic phase high-order modes' variance, obtained with the classical pre-compensation method. We observe in every turbulence condition that the phase error due to the cone effect is negligible (of the order of $10^{-2} \mathrm{rad}^2$ or less) and much smaller than the plane wave turbulent phase variance and the anisoplanatic error. This justifies modelling the phase high-order modes using a plane wave formalism.
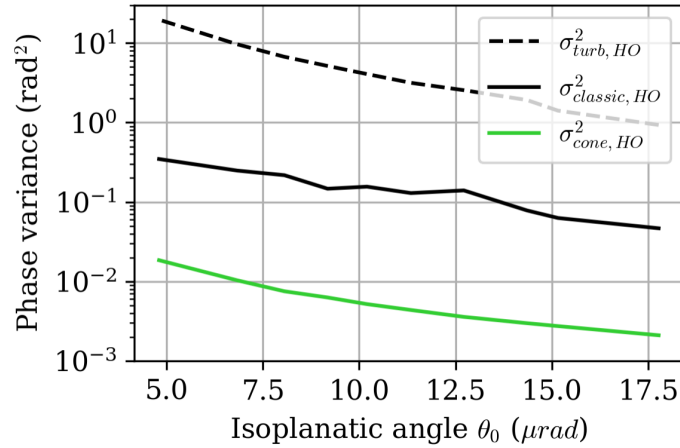
Fig. 5. Phase variance for the phase high order modes function of the isoplanatic angle for the error induced by the cone effect compared to the turbulent phase (black dashed line) and to the error obtained with the classical pre-compensation (black plain line).

4.5. New estimator performance

In this section, we present the results obtained with the new estimator $MMSE_{\Phi\chi,LGS}$ proposed in section 3. We recall that this scenario assumes a static punctual LGS, hence a perfect measurement of the high order modes of the phase at the PAA. The estimator performance is therefore an upper bound of the achievable performance. We also assume that the C_n^2 profile is known. The results are compared with the presented benchmark case from section 4.3. We present the tip-tilt and focus modal reduction brought by the new estimator, and then analyse this modal reduction impact on the coupled flux statistics and communication capabilities.

4.5.1. Tip tilt and focus reduction

We plot in Fig. 6 the tip, tilt and focus residual phase variance, applying the different benchmark AO corrections, and the new estimated AO correction, $MMSE_{\Phi\chi,LGS}$. We recall that in the standard LGS correction case, we assume that the tip, tilt and focus are sensed on the satellite downlink beacon and the high-orders to be perfectly corrected. Hence, the standard LGS tip, tilt and focus corrected variances are identical to the classic correction variances depicted on the plots.

In the first row, we plot the tip reduction function of the isoplanatic angle θ_0 (in absolute value in the first column, and the percentage of anisoplanatic mode reduction in the second column). The method $MMSE_{\Phi\chi}$ is already shown to greatly reduce the tip compared to the classical correction, for all turbulence cases, with a reduction fluctuating around 50%. Similarly, the method $MMSE_{\Phi\chi,LGS}$ further decreases the tip variance by approximately 70%.

In the second row, we also observe a great tilt reduction using the $MMSE_{\Phi\chi,LGS}$ method compared to the former $MMSE_{\Phi\chi}$ and classical method. The method $MMSE_{\Phi\chi}$ is shown to reduce the classical AO tilt variance by 25%, for all turbulence cases, and the $MMSE_{\Phi\chi,LGS}$ further reduces the classic tilt variance by 50%. We note that the asymmetry in the tip and tilt values is induced by the link geometry, in particular the orientation of the PAA that leads to a greater tip value [22].

The greater mode reduction improvement can be observed on the focus, in the third row, with a 75% reduction of the classic AO focus variance brought by the new estimator, compared to a former 50% reduction brought by the $MMSE_{\Phi\chi}$ estimator. This can be explained by a greater
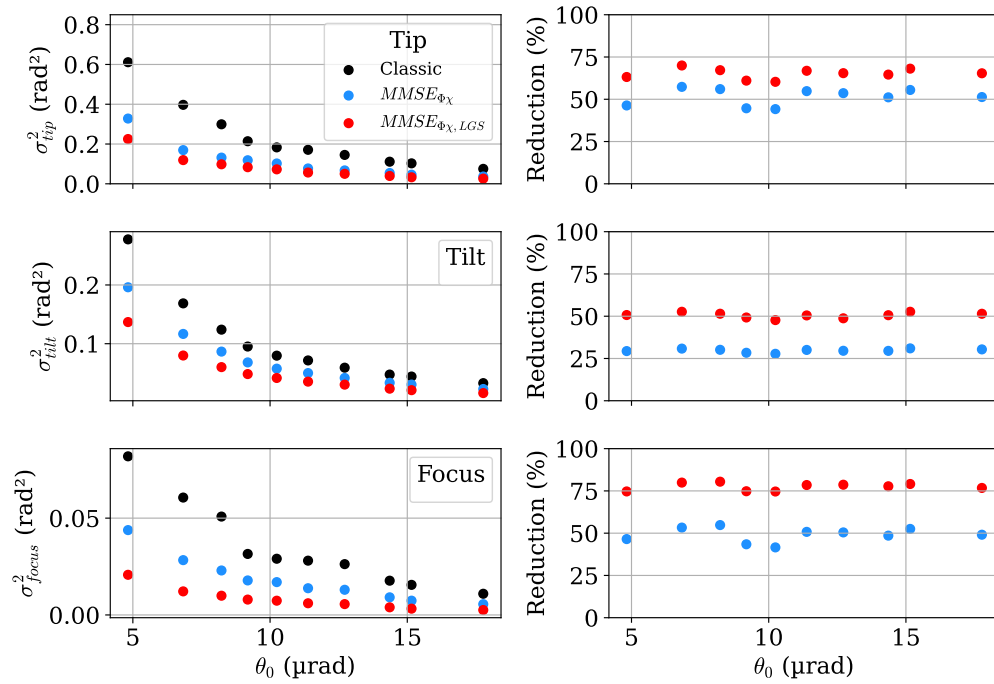
Fig. 6. Tip tilt and focus variance function of the isoplanatic angle (corresponding to the different MOSPAR profiles), in absolute value (first column) and reduction compared to the classical pre-compensation method (second column), for the benchmark cases and the new estimator $MMSE_{\Phi\chi,LGS}$, in red. The first row corresponds to the tip, the second to the tilt and the third to the focus.

correlation of the focus at PAA with high order modes of the phase at PAA, than the tip and tilt correlation to high order modes at PAA. Indeed, the focus correlation to the 11th Zernike mode equals -0.5 while both the tip and tilt correlation to the 8th and 7th Zernike mode equal -0.35.

Finally, we comment on the variance reduction fluctuation function of θ_0 that can be observed for both the $MMSE_{\Phi\chi}$ and $MMSE_{\Phi\chi,LGS}$ estimators, for the tip, tilt and focus estimation. These fluctuations can be explained by the C_n^2 profile distribution and the amount of anisoplanatic error generated at each height. To illustrate this point, we plot in Fig. 7(a) the percentage of tip anisoplanatic error generated at each z for the profile with the worst reduction (MOSPAR 7070) and the best reduction (MOSPAR 9090). We observe in the MOSPAR 7070 case that most of the anisoplanatism is generated in the upper layers (peak around 30 km), while in the MOSPAR 9090 case, the higher contribution is generated around 22 km. Additionally, we plot in Fig. 7(b) the tip reduction in the $MMSE_{\Phi\chi}$ and $MMSE_{\Phi\chi,LGS}$ cases, in function of the percentage of anisoplanatism generated above 28 km. We observe that the variance reduction decreases as the percentage of upper anisoplanatism increases. This validates that the estimator performance is influenced by the vertical distribution of anisoplanatism, which depends on the vertical distribution of the C_n^2 profile.

In Fig. 8, we also plot for the MOSPAR 9090 case the mode variance reduction function of the number of phase high orders sensed by the LGS, compared to the $MMSE_{\Phi\chi}$ method using no LGS measurements, in dashed lines. We observe that sensing four phase radial orders already greatly improves the tip, tilt, and focus estimation. This shows that using a limited number of wavefront sensor sub-apertures, which can be constrained by photometric considerations, still brings gain compared to the method using no LGS.
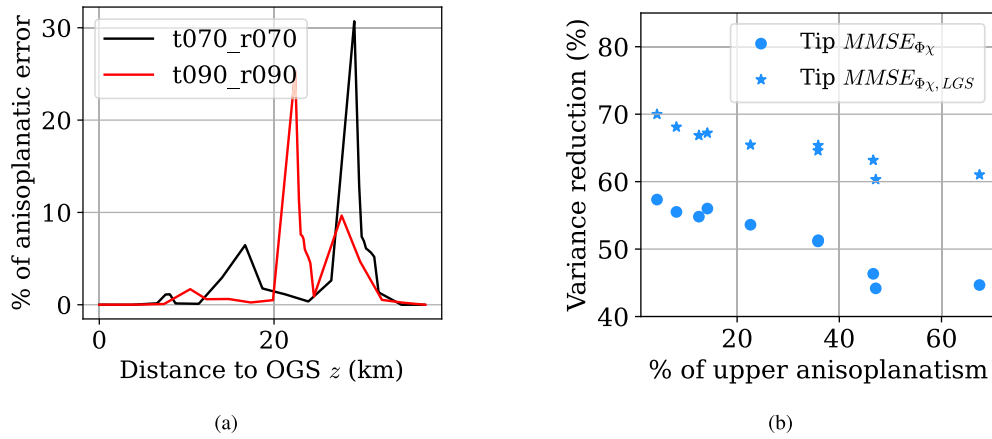
Fig. 7. (a) Percentage of tip anisoplanatism function of the distance to the OGS for the profiles 9090 and 7070 (max and min reductions). (b) Anisoplanatic tip variance reduction function of the percentage of anisoplanatism induced by layers above 28 km for estimators $MMSE_{\Phi\chi}$ and $MMSE_{\Phi\chi,LGS}$.
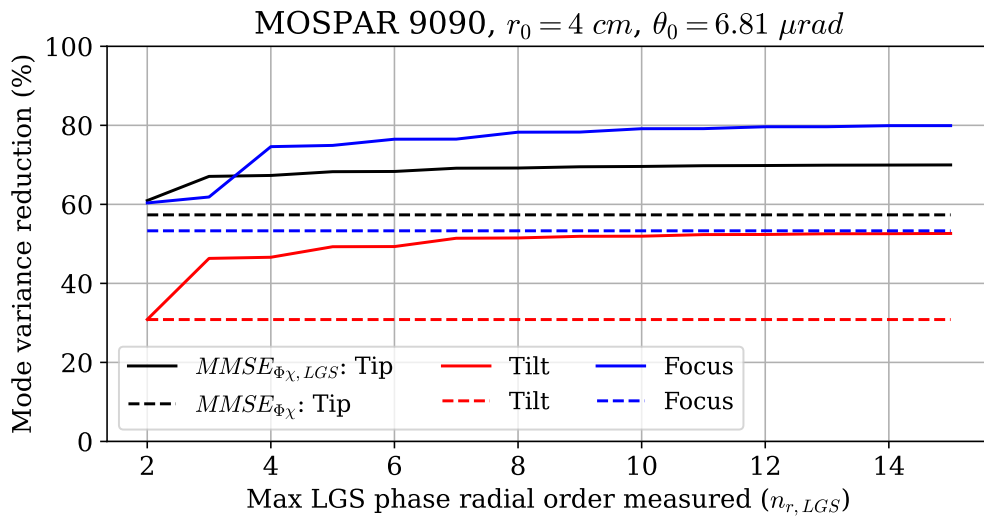

Fig. 8. Tip tilt and focus variance reduction function of the maximum LGS mode radial order sensed and used in the estimation (plain lines), compared to the estimation $MMSE_{\Phi\chi}$ without LGS (dashed lines), in the MOSPAR 9090 case.

To conclude, we observe an important reduction of the tip-tilt and focus when the new estimator $MMSE_{\Phi\chi,LGS}$ is applied, whose reduction rate is quasi-independent of the turbulence conditions. This small dependency can be explained by the distribution of the anisoplanatic error along the line of sight, which depends on the link geometry and the C_n^2 profile distribution. We observe this same quasi-constant reduction compared to the atmospheric conditions concerning the $MMSE_{\Phi\chi}$ method. We also observe a great reduction gain with few LGS phase high order modes sensed. Thanks to the important reduction of the tip, tilt and focus, even in severe angular decorrelation conditions, we expect the new estimator to greatly improve the coupled flux statistics. In the following, we consider that $N_{LGS} = N_{AO} = 136$.

4.5.2. Impact on the coupled flux

Previously, we demonstrated that the new phase estimator greatly reduced the tip-tilt and focus pre-compensation error. We now analyse the coupled flux statistics, computed from 50000 statistically independent coupled flux samples generated thanks to the pseudo-analytical model described in section 4.1, for all the MOSPAR profiles described.

We plot in Fig. 9 the mean value of the coupled flux $<f>$ (left), the normalised coupled flux variance (also referred to as the scintillation index in the literature [44]), denoted $VAR(f)/<f>^2$ (centre), and the coupled flux threshold f_{th} such that $P(f \leq f_{th}) = 10^{-3}$ (meaning that 0.01% of the coupled flux values are below this threshold), function of the isoplanatic angle. The results are plotted for the classical pre-compensation case (black), the LGS case (green), the $MMSE_{\Phi\chi}$ case (blue), and the new proposed estimator $MMSE_{\Phi\chi,LGS}$ (red).

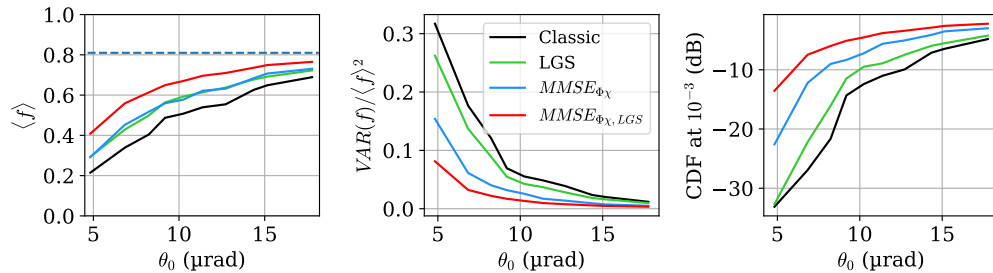**Fig. 9.** On the left, mean coupled flux value function of the isoplanatic angle θ_0, in the middle, normalised coupled flux variance function of θ_0, on the right, coupled flux CDF threshold at probability 10^{-3}, for all MOSPAR profiles and all correction cases.

Analysing the mean value of $<f>$, we observe that all the methods' mean value degrades when the isoplanatic angle decreases. As described in Fig. 3, the turbulence strength also increases when θ_0 decreases. Hence, this global behaviour can be interpreted as a fitting error increasing with r_0. Additionally, we observe a similar mean value for the $MMSE_{\Phi\chi}$ method and the LGS method. This is surprising, as they have a completely different modal phase variance distribution. Finally, the best mean value for all atmospheric conditions is obtained with the new proposed estimator, which doubles the signal mean value in the worst atmospheric conditions (MOSPAR 9999).

Regarding the normalised coupled flux variance, we observe that for every turbulence case, the signal fluctuations are greatest in the classical case, followed by the LGS case. A performance gap is observed between the LGS and the $MMSE_{\Phi\chi}$ case. This highlights the impact of reducing the low-order modes variance, which in turn decreases the signal variance. Ultimately, the new estimator achieves the best performance, as it perfectly corrects the high-order modes, similar to the LGS case, while also reducing the tip, tilt, and focus variance compared to all other methods.

In the most severe turbulence case, the signal fluctuations are shown to be reduced by a factor of three compared to the classical AO correction.

Finally, we analyse on the graph on the right the value of the coupled flux threshold f_{th} in dBs, such that 0.1% of the coupled flux occurrences are below this threshold, as a function of the isoplanatic angle. We observe that the improvement provided by the LGS case with anisoplanatic tip, tilt, and focus is minor compared to the gains achieved by the MMSE methods. In particular, in the worst-case scenario, when θ_0 is the smallest, we observe that the LGS case brings negligible gain compared to the classical method, whereas the $MMSE_{\Phi\chi}$ estimator brings a 10 dB gain and the $MMSE_{\Phi\chi,LGS}$ estimator a 19 dB gain. Overall, with the new estimator, the minimum coupled flux threshold reported across the studied atmospheric conditions is -13 dB.

We also plot the probability density functions and cumulative density functions of the coupled flux for the turbulence profiles MOSPAR 5050, 9090, and 9999, in Fig. 10. In the case MOSPAR 5050, all the pre-compensation methods seem to follow the same statistical law, with different means and variances. However, when the turbulence strength increases, the statistics of the coupled flux obtained with the classical and standard LGS case seem to follow a different statistical law, whose fade occurrence probability is higher. This is a direct consequence of the beam wander induced by the residual anisoplanatic tip tilt, that is not corrected on either of these two cases. On the contrary, the new estimated method $MMSE_{\Phi\chi,LGS}$ allows obtaining coupled flux statistics more stable with the changing atmospheric conditions. This stability is achieved by limiting the residual variance in tip, tilt, and focus.
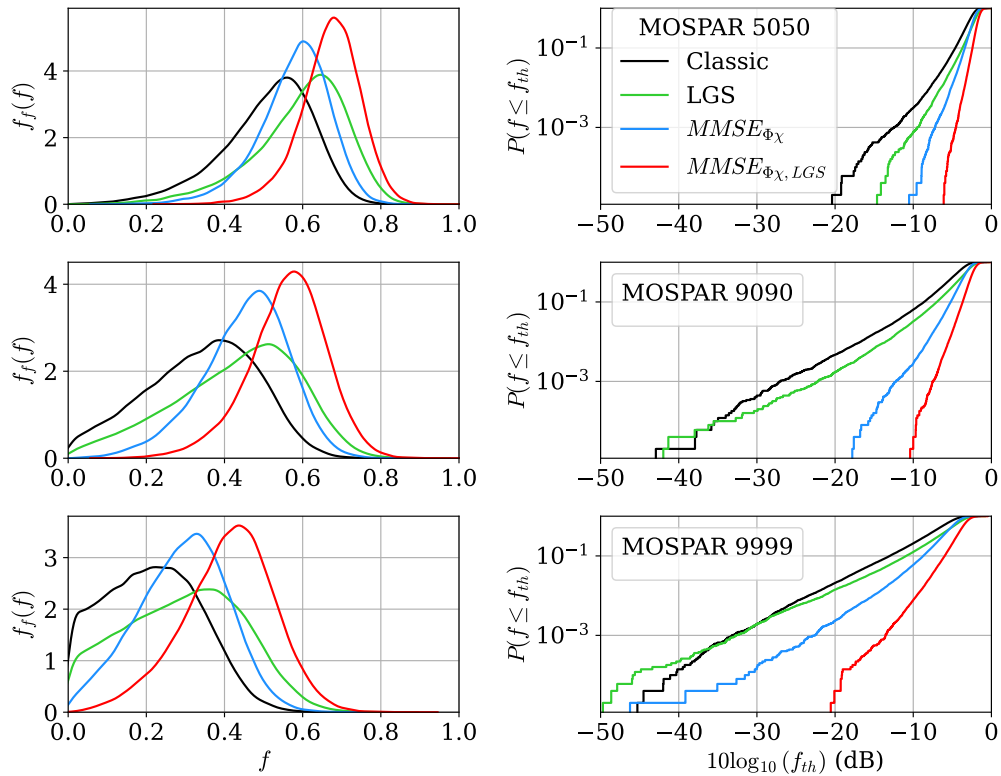

Fig. 10. Probability density function (first column) and cumulative density function (second column) of the coupled flux, for the profiles MOSPAR 5050 (first row), 9090 (second row) and 9999 (third row), for the benchmark pre-compensation methods and the new estimator (red).

4.5.3. Telecommunication performance improvement

Finally, we assess the estimator's impact on telecommunication performance by evaluating the theoretical transmission limits, or capacity, of the different channels. As stated by the noisy coding theorem of Shannon [45], for a given capacity C, if the information rate r is strictly below C, then a code enables an error-free transmission at this code rate. We recall that, as the LGS system and AO correction are idealised, the computed capacity only depicts an upper bound of the achievable performance, and would be reduced in a real-world implementation. This remains relevant as it indicates which data rates are prohibited under specific atmospheric conditions.

For an AWGN channel with bandwidth and power constraints, the capacity is defined as [46]:

$$C_0 = B \log_2(1 + SNR_0) = B \log_2(1 + P/N_0 B) \text{ (bit/s)} \tag{29}$$

where B is the received signal bandwidth, P is the average emitted power, and $N_0/2$ is the noise power spectral density. In the case of the pre-compensated ground-to-satellite channel, the SNR becomes:

$$SNR = f L_{cst} SNR_0 \tag{30}$$

as the received power onboard the satellite is affected by losses assumed constant L_{cst}, related to physical effects such as molecular absorption, geometrical losses or system internal losses [39], and the random losses f induced by the atmospheric turbulence. Therefore, we express the capacity per unit of bandwidth as:

$$\frac{C}{B} = \log_2(1 + SNR(f)) \text{ (bit/s/Hz)}. \tag{31}$$

We note that the capacity per unit of bandwidth is a function of the random variable f. Hence, it is also a random variable. Therefore, as at a fixed code rate, there is a non-zero probability that $C < r$, a more relevant metric is the outage probability defined as:

$$P_{outage} = P(C(f) < r) \tag{32}$$

Finally, we define the ϵ-outage capacity [47], which defines the rate $r = C_\epsilon$ threshold such that there is an outage probability of ϵ. It is the achievable capacity with the reliability rate ϵ. It writes:

$$P_{outage} = P(C(f) < C_\epsilon) = \epsilon \tag{33}$$

Hence, we study the ϵ-outage capacity for an $\epsilon = 10^{-3}$. We plot the ϵ-outage capacity per unit of bandwidth on the top of Fig. 11, in function of the isoplanatic angle θ_0, for all the pre-compensation methods and three different electrical SNR before atmosphere attenuation issued from the link budget in [48], and in agreement with previous studies [49]. We also plot the AWGN capacity in dotted lines, for every SNR. At the bottom, we plot the capacity loss compared to the AWGN capacity, function of θ_0. We observe, for every SNR value, that the new proposed estimator improves the ϵ-outage capacity compared to the other pre-compensation methods. In the more severe turbulence scenario, the ϵ-outage capacity is shown to be very limited (between 0.5 and 1.8 bit per second per Hz, for the three studied SNR). However, this capacity achieved with the new proposed estimator is higher than the capacity in the classical and standard LGS cases, which are close to 0. In the median turbulence cases ($\theta_0 = 10\mu rad$) for SNR=10 dB, we observe that 60% of the AWGN capacity can be achieved using the new $MMSE_{\Phi_\chi,LGS}$ method, whereas using the standard LGS or the classical AO methods allow only to achieve 30% and 20% of the AWGN capacity. Finally, in mild turbulence conditions, the new estimator allows approaching the AWGN capacities, for all the given SNR values.

In conclusion, the new estimator enhances the channel capacity that can be achieved 99.9% of the time compared to classical AO pre-compensation, enabling data transmission even under the most severe turbulence conditions.
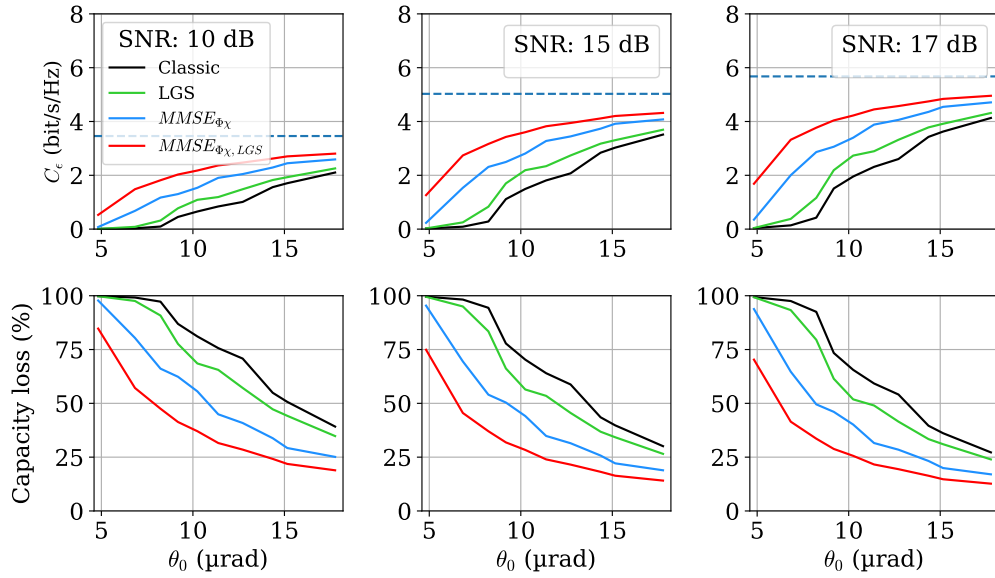
Fig. 11. On the top: ϵ-outage capacity function of the isoplanatic angle θ_0 for the SNR 10 dB, 15 dB and 17 dB. At the bottom: Capacity loss in percentage compared to the AWGN capacity.

5. Conclusion

In this article, we presented a novel approach to estimate the tip, the tilt, and the focus at the point-ahead angle. In this aim, we developed an MMSE estimator that jointly uses measurements and statistical priors from the available on-axis downlink phase, log-amplitude, and off-axis phase high-order modes sensed by the LGS. We derived the analytical expression of the new estimator and evaluated its efficiency compared to state-of-the-art pre-compensation methods, including classical pre-compensation, standard LGS-based pre-compensation, and the $MMSE_{\Phi\chi}$ methods. We evaluate the improvements in the coupled flux statistics and the achievable capacity with a reliability rate of 99.9%. We note that these results are an upper bound of the performance that can be achieved with this technique, as the LGS system is idealised.

We show in multiple atmospheric conditions that the pre-compensation error on the tip, tilt and focus is reduced by 70%, 50% and 75% of their initial values. This phase error reduction is improved compared with our first proposed method, relying only on the downlink beam measurements, showing that the LGS phase high-order knowledge brings valuable information to the estimation. This phase estimation improvement is shown to improve the statistics of the coupled flux with respect to all state-of-the-art methods, improving the mean value of the coupled flux attenuation, reducing the scintillation index of the signal and decreasing the number of deep fades, for all considered atmospheric conditions. We also show that the capacity that can be achieved 99.9% of the time is improved in every turbulence condition. In particular, in very severe atmospheric conditions, the AWGN channel capacity loss is reduced up to 30%, compared to the classical pre-compensation capacity loss. This shows that this method could allow for higher data rates in every atmospheric turbulence condition and extend the global availability window of a given optical ground station.

In this study, we establish an upper bound on the performance that can be achieved by jointly using the available downlink beam and LGS high-order phase measurements to estimate the ground-to-GEO pre-compensation phase. It is referred to as an upper bound as we assume perfect

measurements of the LGS phase high-order modes and perfect knowledge of the C_n^2 profile. Future work will include a refined LGS model that considers experimental constraints, such as the LGS residual jitter, spot extension and the measurement error on the high order modes of the LGS. Additionally, to experimentally demonstrate the efficiency of this estimator, the sensitivity of its performance to a measured C_n^2 profile will need to be studied. In particular, examining the sensitivity to the profile's spatial and temporal resolution will help specify the requirements for the profiling instruments or methods to use. These studies will pave the way toward an experimental demonstration of the estimation concept on a system incorporating AO and LGS.

References

1. C. A. Vasko, P.-D. Arapoglou, G. Acar, *et al.*, "Optical high-speed data network in space-an update on hydron's system concept," in *2022 IEEE International Conference on Space Optical Systems and Applications (ICSOS)*, (IEEE, 2022), pp. 7–13.
2. R. Boddeda, D. Romero Arrieta, S. Almonacil, *et al.*, "Achievable capacity of geostationary-ground optical links," J. Lightwave Technol. **41**(12), 3717–3725 (2023).
3. R. K. Tyson, "Adaptive optics and ground-to-space laser communications," Appl. Opt. **35**(19), 3640–3646 (1996).
4. A. Montmerle-Bonnefois, M.-T. Velluet, M. Cissé, *et al.*, "Feasibility demonstration of ao pre-compensation for geo feeder links in a relevant environment," Opt. Express **30**(26), 47179–47198 (2022).
5. A. Brady, C. Rössler, N. Leonhard, *et al.*, "Validation of pre-compensation under point-ahead-angle in a 1 km free-space propagation experiment," Opt. Express **27**(13), 17840–17850 (2019).
6. N. Leonhard, R. Berlich, S. Minardi, *et al.*, "Real-time adaptive optics testbed to investigate point-ahead angle in pre-compensation of earth-to-geo optical communication," Opt. Express **24**(12), 13157–13172 (2016).
7. R. Saathof, R. Den Breeje, W. Klop, *et al.*, "Pre-correction adaptive optics performance for a 10 km laser link," in *Free-Space Laser Communications XXXI*, vol. 10910 (SPIE, 2019), pp. 325–331.
8. I. R. Hristovski, A. R. Campelo, B. Femenía-Castella, *et al.*, "Pre-distortion adaptive optics: experimental results from bi-directional tracking links between dlr's optical ground station and alphasat's tdp-1 terminal," in *Free-Space Laser Communications XXXVI*, vol. 12877 (SPIE, 2024), pp. 328–336.
9. K. Kudielka, E. Fischer, T. Berkefeld, *et al.*, "Successful first optical feeder link demonstration between a ground station and a GEO satellite applying adaptive optics pre-compensation ("Alpha-Up")," in *COAT2023*, (Durham, United Kingdom, 2023).
10. J. Osborn, M. J. Townson, O. J. D. Farley, *et al.*, "Adaptive optics pre-compensated laser uplink to leo and geo," Opt. Express **29**(4), 6113–6132 (2021).
11. P. Lognoné, J.-M. Conan, G. Rekaya, *et al.*, "Two-aperture measurements for geo-feeder adaptive optics pre-compensation optimization," Opt. Lett. **48**(17), 4550–4553 (2023).
12. R. Biasi, D. B. Calia, M. Centrone, *et al.*, "Alasca: the esa laser guide star adaptive optics optical feeder link demonstrator facility," in *International Conference on Space Optics-ICSO 2022*, vol. 12777 (SPIE, 2023), pp. 2219–2236.
13. M. Cockram, N. M. Rey, A. Gilling, *et al.*, "Using observational data of double stars to assess the feasibility of tip-tilt retrieval on the downlink signal for uplink pre-compensation in free space optical communications," in *International Conference on Space Optics-ICSO 2022*, vol. 12777 (SPIE, 2023), pp. 1889–1900.
14. A. P. Reeves, N. Ageorges, D. Kampf, *et al.*, "Geostar: demonstration of laser guide star adaptive optics for free space optical communications," in *Free-Space Laser Communications XXXVI*, vol. 12877 (SPIE, 2024), pp. 482–491.
15. F. Rigaut and E. Gendron, "Laser guide star in adaptive optics : the tilt determination problem," Astron. Astrophys. **261**, 677–684 (1992).
16. R. Ragazzoni, "Propagation delay of a laser beacon as a tool to retrieve absolute tilt measurements," The Astrophys. J. **465**(1), L73–L75 (1996).
17. N. Martinez, L. F. R. Ramos, A. Alonso, *et al.*, "Plenoptic wavefront sensor for free-space optical communications," in *Free-Space Laser Communications XXXIV*, vol. 11993 (SPIE, 2022), pp. 234–245.
18. E. Holdorf and N. Martinez-Rey, "Horizontal sodium density variations for laser guide star tip-tilt measurements," Mon. Not. R. Astron. Soc. **531**(3), 3159–3167 (2024).
19. R. Foy, J.-P. Pique, A. D. Petit, *et al.*, "Polychromatic guide star: feasibility study," in *High-Power Laser Ablation III*, vol. 4065 (SPIE, 2000), pp. 312–323.

20. D. B. Calia, J. Osborn, P. Haguenauer, *et al.*, "Canapy: Lgs-ao experimental facility for visible wavelengths," in *Adaptive Optics Systems VIII*, vol. 12185 (SPIE, 2022), p. 121857L.

21. M. R. Whiteley, B. M. Welsh, and M. C. Roggemann, "Incorporating higher-order modal measurements in tilt estimation: natural and laser guide star applications," Appl. Opt. **37**(36), 8287–8296 (1998).

22. P. Lognoné, J.-M. Conan, G. Rekaya, *et al.*, "Phase estimation at the point-ahead angle for ao pre-compensated ground to geo satellite telecoms," Opt. Express **31**(3), 3441–3458 (2023).

23. R. J. Noll, "Zernike polynomials and atmospheric turbulence," J. Opt. Soc. Am. **66**(3), 207–211 (1976).

24. C. Robert, J.-M. Conan, and P. Wolf, "Impact of turbulence on high-precision ground-satellite frequency transfer with two-way coherent optical links," Phys. Rev. A **93**(3), 033860 (2016).

25. O. J. D. Farley, M. J. Townson, and J. Osborn, "Fast: Fourier domain adaptive optics simulation tool for bidirectional ground-space optical links through atmospheric turbulence," Opt. Express **30**(13), 23050 (2022).

26. J. H. Shapiro and A. L. Puryear, "Reciprocity-enhanced optical communication through atmospheric turbulence-part i: Reciprocity proofs and far-field power transfer optimization," J. Opt. Commun. Netw. **4**(12), 947–954 (2012).

27. P. Lognoné, J.-M. Conan, L. Paillier, *et al.*, "Channel model of a ground to satellite optical link pre-compensated by adaptive optics," in *Signal Processing in Photonic Communications*, (Optica Publishing Group, 2022), pp. SpTu3G–3.

28. D. B. Calia, M. Centrone, E. Pinna, *et al.*, "Canapy: Satcomm lgs-ao experimental platform with laser uplink pre-compensation," in *International Conference on Space Optics-ICSO 2020*, vol. 11852 (SPIE, 2021), pp. 536–546.

29. R. K. Tyson, *Introduction to adaptive optics*, vol. 41 (SPIE, 2000).

30. S. M. Kay, *Fundamentals of statistical signal processing: estimation theory* (Prentice-Hall, 1993).

31. L. Canuet, N. Védrenne, J.-M. Conan, *et al.*, "Statistical properties of single-mode fiber coupling of satellite-to-ground laser links partially corrected by adaptive optics," J. Opt. Soc. Am. A **35**(1), 148–162 (2018).

32. F. Mahé, "Application d'un modèle atmosphérique à l'étude des fluctuations d'indice de réfraction dans la couche limite : influence de la scintillation sur l'analyse de front d'onde," Ph.D. thesis (2000).

33. R. J. Sasiela, "Basic equations for wave propagation in turbulence," in *Electromagnetic Wave Propagation in Turbulence*, (Springer, 1994), pp. 19–46.

34. D. L. Fried, "Aperture averaging of scintillation," J. Opt. Soc. Am. **57**(2), 169–175 (1967).

35. F. Mahe, V. Michau, G. Rousset, *et al.*, "Scintillation effects on wavefront sensing in the rytov regime," in *Propagation and Imaging through the Atmosphere IV*, vol. 4125 (SPIE, 2000), pp. 77–86.

36. F. Roddier, *Adaptive Optics in Astronomy* (Cambridge University, 1999).

37. J.-M. Conan, "Etude de la correction partielle en optique adaptative," Ph.D. thesis, Paris 11 (1994).

38. V. Marulanda Acosta, D. Dequal, M. Schiavon, *et al.*, "Analysis of satellite-to-ground quantum key distribution with adaptive optics," New J. Phys. **26**(2), 023039 (2024).

39. N. Vedrenne, C. Petit, A. Montmerle-Bonnefois, *et al.*, "Performance analysis of an adaptive optics based optical feeder link ground station," in *International Conference on Space Optics-ICSO 2020*, vol. 11852 (SPIE, 2021), pp. 527–535.

40. A. Ziad, F. Blary, J. Borgnino, *et al.*, "First results of the pml monitor of atmospheric turbulence profile with high vertical resolution," Astron. Astrophys. **559**, L6 (2013).

41. S. Esposito, A. Riccardi, and R. Ragazzoni, "Focus anisoplanatism effects on tip–tilt compensation for adaptive optics with use of a sodium laser beacon as a tracking reference," J. Opt. Soc. Am. A **13**(9), 1916–1923 (1996).

42. G. A. Tyler, "Rapid evaluation of d 0: the effective diameter of a laser-guide-star adaptive-optics system," J. Opt. Soc. Am. A **11**(1), 325–338 (1994).

43. F. Chassat, "Optical propagation through atmospheric turbulence. Model analysis of anisoplanatism and application to adaptive optics," Ph.D. thesis, Office National d'Etudes et de Recherche Aerospatiale, France (1992).

44. L. C. Andrews, R. L. Phillips, C. Y. Hopen, *et al.*, "Theory of optical scintillation," J. Opt. Soc. Am. A **16**(6), 1417–1429 (1999).

45. C. E. Shannon, "Communication in the presence of noise," Proc. IRE **37**(1), 10–21 (1949).

46. J. G. Proakis, *Digital communications* (McGraw-Hill, 2008).

47. A. Belmonte and J. M. Kahn, "Capacity of coherent free-space optical links using diversity-combining techniques," Opt. Express **17**(15), 12601–12611 (2009).

48. P. Lognoné, "Optimization of high data rate ground to satellite links pre-compensated by adaptive optics," Ph.D. thesis, Institut Polytechnique de Paris (2023).

49. R. Barrios, S. Dimitrov, R. Mata-Calvo, *et al.*, "Link budget assessment for geo feeder links based on optical technology," Int. J. Satell. Commun. Netw. **39**(2), 160–177 (2021).

50. J. Osborn, R. W. Wilson, M. Sarazin, *et al.*, "Optical turbulence profiling with Stereo-SCIDAR for VLT and ELT," Mon. Not. R. Astron. Soc. **478**(1), 825–834 (2018).